44th AIAA Aerospace Sciences Meeting and Exhibit
9 - 12 January 2006, Reno, Nevada

AIAA 2006-1256

Zonal Hybrid RANS-LES Method for Static and Oscillating Airfoils and Wings

M. Sánchez-Rocha*, M. Kırtaş†and S. Menon‡
Georgia Institute of Technology, Atlanta G.A., 30332-0150, U.S.A.

The present work evaluates the potential of a hybrid RANS-LES method to predict the unsteady flow over airfoils in static and oscillating motion. The method implemented (hereafter termed HRLES) blends the $k-\omega$ SST RANS model with a localized dynamic k^{sgs} one-equation LES model (LDKM). The unsteady 2D and 3D flow over a NACA 0015 airfoil is computed to evaluate the model performance. The aerodynamic characteristics of the static configuration are in reasonable agreement with experimental results. For the oscillating case, three conditions are simulated: attached flow, mild stall and deep stall. Two-dimensional simulations are conducted for the three dynamic stall conditions, and only the deep stall case is simulated in 3D so far. Overall, the unsteady loads for the attached and mild stall cases show good agreement with experiments. For the mild and the deep stall cases, the HRLES is able to predict flow separation and vortex shedding during the downstroke. In general, these results demonstrate the potential of hybrid methods to correctly simulate complex high Reynolds number flows encountered in aerodynamic applications.

Nomenclature

Cp	= specific heat at constant pressure	t	= time
C_p	= pressure coefficient	T	= temperature
e	= internal energy	T'	= time average interval
E	= total energy	u_i	= velocity vector
E_j^{turb}	= turbulent energy flux vector	x_i	= position vector
G	= filter function	μ	= molecular viscosity
k	= modeled kinetic energy	ρ	= density
Pr	= molecular Prandtl number	τ_{ij}	= molecular stress tensor
Pr_T	= turbulent Prandtl number	τ_{ij}^{turb}	= turbulent stress tensor
$Prod$	= production	ϕ	= dummy variable
q_i	= heat flux vector	ω	= specific dissipation rate
p	= pressure	ψ	= dummy variable

Superscript and subscripts

sgs	= subgrid scale	$rans$	= Reynolds Averaged Navier-Stokes
hyb	= hybrid	$trans$	= transport
src	= source	$turb$	= turbulence, RANS or LES
$rans/sgs$	= RANS or LES		

*Graduate student, student member.
†Graduate student.
‡Professor, Associate Fellow, AIAA.

I. Introduction

DYNAMIC stall is a complex phenomenon encountered in many aerodynamic applications like helicopter rotors, turbomachinery, aircraft during maneuver and wind turbines. In oscillating wings, dynamic stall can dramatically increase the aerodynamic loads and the stall angle encountered in steady state conditions. The unsteady boundary layer separation and reattachment induced by the oscillation generates an asymmetric flow during the cycle. This asymmetry is characterized by a hysteresis in the unsteady aerodynamic loads. Helicopter rotors are severely affected by these unsteady loads. Consequently, optimal structural designs require accurate unsteady flow solutions. However, current Reynolds Averaged Navier-Stokes (RANS) methods can only predict cycle-averaged unsteady loads. This level of accuracy may be enough for a first approximation. Nevertheless, Piziali[1] stressed in his experimental investigation: "Cycle-averaged data may or may not be representative of individual cycles. In many cases, the cycle-to-cycle variation can be significant." Whereas, cycle-averaged data may be smooth, individual cycles may present important peaks and deviation from mean values that cannot be ignored in the final design. Therefore, next generation turbulence models must predict cycle-averaged experimental data only as an average of individual unsteady cycles.

Usually, when unsteady flow solutions are required, Large Eddy Simulation (LES) has been proposed to replace RANS methods. Nevertheless, for aerodynamic flows of engineering application, LES still requires a tremendous amount of computer resources, for examples, Mary and Sagaut[2] simulated the 3D LES (attached) flow over the Aerospatiale airfoil at $Re = 2 \times 10^6$ and $\alpha = 13$. This particular simulation required grids of around 2.2 and 7.2 millions grid points. Mellen et al.[3] reported the results of the joint European LESFOIL project where LES simulations were conducted for the same Aerospatiale airfoil. Among their results, the best predictions were achieved with grids around 18 millions grid points. Based on these experiences and the current computational resources, LES is not yet feasible to be used on a regular basis to design industrial aerodynamic flows.

The main limitation of LES in aerodynamic flows is that the walls have to be accurately resolved while keeping reasonable grid cells aspect ratios. This constraint imposes a tremendous grid requirement, as previously mentioned. In order to alleviate the LES near-wall resolution requriments, it has been proposed to use RANS models in the near-wall region, whereas, away from it, LES closure is used. This approach has been named hybrid RANS-LES methods. Different hybrid RANS-LES methods have been proposed. As a first approximation, Speziale[4] proposed to bridge RANS and LES methods by means of a reduction in the RANS stress tensor (τ_{ij}^{rans}). The transition between RANS and LES is controlled by the grid size (Δ) and the Kolmogorov microscale (η_k): $\tau_{ij} = \left[1 - e^{-\beta\Delta/\eta_k}\right]^n \tau_{ij}^{rans}$, here β and n are model constants. A second approach, that have become popular, is the Detached Eddy Simulation (DES) by Spalart et al.[5] DES is a hybrid RANS-LES method based on the Spalart-Allmaras[6] one equation model. Depending on the grid geometry, DES switches from RANS near the wall to a pseudo Smagorinky LES closure away from it. Unfortunately, the transition between RANS and LES is controlled by grid geometry and not by turbulence quantities. More recently Xiao et al.[7,8] developed a zonal hybrid RANS-LES approach. This zonal approach uses a blending function to merge RANS and LES equations and may also depend on local flow properties, besides wall distance and grid spacing.

In this investigation, we present an alternative way to pursue hybrid RANS-LES simulations. Here, we propose a procedure that can be applied not only in the turbulence model equations but also in any transport equation used in Computational Fluid Dynamics. Following this, we postulate the governing equations required in hybrid RANS-LES simulations. Then the present methodology is applied to several high Reynolds number airfoil/wing flows encountered in aerodynamic applications. In particular, the potential of the present formulation is explored by simulating a 3D pitching wing case. To the present authors' best knowledge, this is the first hybrid RANS-LES simulation of a pitching wing in realistic flow conditions.

II. Hybrid RANS-LES (HRLES) Formulation

This section presents the governing equations for RANS and LES methods. The equations are cast in a form that can be interpreted in either RANS or LES frame. Later on, the HRLES governing equations are postulated, and finally, the RANS and LES model implementations are described.

A. HRLES Governing Equations

To formulate the RANS and LES equations, the compressible Navier-Stokes equations have to be either Favre averaged or Favre filtered (refer to Eqs. (1-2), for definitions). If no interpretation is given to the Favre operator, the final equations can be written in a generic way, leaving the unclosed terms undefined until the Favre operator is defined. Thus, Eqs. (3 to 5) represent the generic compressible mass, momentum and energy conservation equations after Favre operation. Likewise, we can formulate a generic transport "k" equation model that can be either RANS "k" or LES "k^{sgs}" (Eq. (7)). The set of operators and equations are presented bellow.

- Time average and space filter operators:

$$\overline{\phi}_{rans} = \lim_{T'\to\infty} \frac{1}{T'} \int_t^{t+T'} \phi dt, \quad \overline{\phi}_{sgs} = \int \phi(x-r,t)G(r,x)dr, \tag{1}$$

- Favre average and filter operators:

$$\widetilde{\phi}_{rans} = \frac{\lim_{T'\to\infty} \frac{1}{T'} \int_t^{t+T'} \rho\phi dt}{\lim_{T'\to\infty} \frac{1}{T'} \int_0^{T'} \rho dt}, \quad \widetilde{\phi}_{sgs} = \frac{\int \rho(x-r,t)\phi(x-r,t)G(r,x)dr}{\int \rho(x-r,t)G(r,x)} dr, \tag{2}$$

- Generic compressible Navier-Stokes equations:

$$\frac{\partial \bar{\rho}}{\partial t} + \frac{\partial}{\partial x_j}(\bar{\rho}\widetilde{u}_j) = 0 \tag{3}$$

$$\frac{\partial}{\partial t}(\bar{\rho}\widetilde{u}_i) + \frac{\partial}{\partial x_j}(\bar{\rho}\widetilde{u}_j\widetilde{u}_i) = \frac{\partial}{\partial x_j}(-\overline{p}\delta_{ij} + \widetilde{\tau}_{ji}) + \frac{\partial}{\partial x_j}(\tau_{ji}^{turb}) \tag{4}$$

$$\frac{\partial}{\partial t}(\bar{\rho}\widetilde{E}) + \frac{\partial}{\partial x_j}(\bar{\rho}\widetilde{u}_j\widetilde{E}) = \frac{\partial}{\partial x_j}\left[\widetilde{u}_i(\widetilde{\tau}_{ij} - p\delta_{ij}) - \widetilde{q}_j\right] + \frac{\partial}{\partial x_j}(E_j^{turb}) \tag{5}$$

$$\widetilde{E} = \widetilde{e} + \frac{1}{2}\widetilde{u}_i\widetilde{u}_i + k^{rans/sgs}, \quad \widetilde{\tau}_{ij} = \widetilde{\mu}(\widetilde{T})\Big(\frac{\partial \widetilde{u}_i}{\partial x_j} + \frac{\partial \widetilde{u}_j}{\partial x_i} - \frac{2}{3}\frac{\partial \widetilde{u}_k}{\partial x_k}\delta_{ij}\Big), \quad q_j = -\frac{C_p\widetilde{\mu}(\widetilde{T})}{Pr}\frac{\partial \widetilde{T}}{\partial x_j} \tag{6}$$

- Generic k equation turbulence model:

$$\frac{\partial}{\partial t}(\bar{\rho}k) + \frac{\partial}{\partial x_j}(\bar{\rho}\widetilde{u}_j k) = \frac{\partial}{\partial x_j}(K_{j\ trans}^{turb}) + K_{src}^{turb} \tag{7}$$

Following the work of Baurle et al.,[9] we can linearly merge any well established RANS and LES methods. In addition, Speziale[4] proposed the merging by reducing the Reynolds stress terms. Following these ideas, the postulated generic[a] HRLES governing equation, written in general form including convection, transport, and source terms, is:

$$\begin{aligned}\frac{\partial}{\partial t}(\bar{\rho}\widetilde{\phi}) + \frac{\partial}{\partial x_j}(\bar{\rho}\widetilde{u}_j\widetilde{\phi}) =& \frac{\partial}{\partial x_j}(\phi_j^{trans}) + \widetilde{\phi}_{src} \\ &+ \frac{\partial}{\partial x_j}(\Phi_{j\ trans}^{hyb\ turb}) + \Phi_{src}^{hyb\ turb}\end{aligned} \tag{8}$$

RANS and LES are merged by a modification in the turbulent transport and source terms, Eq.(9). In general, any transport equation used in CFD can be written as Eq.(8), extending the possible range of application for HRLES. In particular for this study, the HRLES formulation include the Navier-Stoke equations and the turbulence "k" equation, $\widetilde{\phi} = \{1,\ \widetilde{u}_i,\ \widetilde{E}, k\}$. The fact that ω must satisfy free stream boundary conditions without an equivalent LES equation precludes the inclusion of ω in the HRLES formulation[b].

$$\Phi_{j\ trans}^{hyb\ turb} = F\Phi_{j\ trans}^{rans} + (1-F)\Phi_{j\ trans}^{sgs}, \quad \Phi_{src}^{hyb\ turb} = F\Phi_{src}^{rans} + (1-F)\Phi_{src}^{sgs}, \tag{9}$$

[a] In order to write any transport equation used in CFD, the corresponding source (if any) and transport terms must be included.

[b] The RANS ω equation is not blended.

B. RANS and LES Model Equations

Based on previous studies in dynamic stall (for example, see Srinivasan et all,[10] Ekaterinaris and Menter,[11] Ko and McCroskey,[12] Ekaterinairs[13,14] and Spentzos et al[15]), we selected the RANS $k-\omega$ SST by Menter,[16] due to its superiority over other RANS methods. For the LES part, we will use the compressible version of the localized dynamic k^{sgs} one-equation model (LDKM) of Kim and Menon.[17] This method has been applied successfully in different applications, as shown in Menon et al.,[18] Kim et al.,[19] Kim and Menon.[17,20] For the sake of completeness, we present the equations for the RANS and LES model.

1. *RANS SST two-equation model*

$$\frac{\partial}{\partial t}(\bar{\rho}k) + \frac{\partial}{\partial x_j}(\bar{\rho}\widetilde{u}_j k) = \tau_{ij}^{rans}\frac{\partial \widetilde{u}_i}{\partial x_j} - \beta^*\rho\omega k + \frac{\partial}{\partial x_j}\Big[(\widetilde{\mu} + \sigma_k\mu_T)\frac{\partial k}{\partial x_j}\Big] \tag{10}$$

$$\begin{aligned}\frac{\partial}{\partial t}(\bar{\rho}\omega) + \frac{\partial}{\partial x_j}(\bar{\rho}\widetilde{u}_j\omega) =& \frac{\gamma\bar{\rho}}{\mu_T}\tau_{ij}^{rans}\frac{\partial \widetilde{u}_i}{\partial x_j} - \beta\rho\omega^2 + \frac{\partial}{\partial x_j}\Big[(\widetilde{\mu} + \sigma_\omega\mu_T)\frac{\partial \omega}{\partial x_j}\Big] \\ &+ 2(1-F_2)\bar{\rho}\sigma_{\omega 2}\frac{1}{\omega}\frac{\partial k}{\partial x_j}\frac{\partial \omega}{\partial x_j}\end{aligned} \tag{11}$$

The model constants (here represented as ψ) are computed from two set of constants (ψ_1 and ψ_2) as follows:

$$\psi = F_2\psi_1 + (1-F_2)\psi_2 \tag{12}$$

Set of constants ψ_1:

$$\begin{aligned}\sigma_{k1} = 0.85, \quad \sigma_{\omega 1} = 0.5, \qquad \beta_1 = 0.075, \qquad a_1 = 0.31, \\ \beta^* = 0.09, \qquad \kappa = 0.41, \qquad \gamma_1 = \frac{\beta_1}{\beta^*} - \frac{\sigma_{\omega 1}\kappa^2}{\sqrt{\beta^*}}\end{aligned} \tag{13}$$

Set of constants ψ_2:

$$\begin{aligned}\sigma_{k2} = 1.0, \qquad \sigma_{\omega 2} = 0.856, \qquad \beta_2 = 0.0828, \\ \beta^* = 0.09, \qquad \kappa = 0.41, \qquad \gamma_2 = \frac{\beta_2}{\beta^*} - \frac{\sigma_{\omega 2}\kappa^2}{\sqrt{\beta^*}}\end{aligned} \tag{14}$$

$$\mu_T = \frac{a_1\bar{\rho}k}{\max(a_1\omega; \Omega F_2)}, \qquad F_2 = \tanh(x^2), \qquad x = \max\Big(2\frac{\sqrt{k}}{0.09\omega y}; \frac{500\nu}{y^2\omega}\Big), \tag{15}$$

$$\tau_{ij}^{rans} = \mu_T\Big(\frac{\partial \widetilde{u}_i}{\partial x_j} + \frac{\partial \widetilde{u}_j}{\partial x_i} - \frac{2}{3}\frac{\partial \widetilde{u}_k}{\partial x_k}\delta_{ij}\Big) - \frac{2}{3}\bar{\rho}k\delta_{ij} \tag{16}$$

Here, Ω is the magnitude of the vorticity vector, ν is the kinematic viscosity, and y is the wall normal distance. In the original paper by Menter,[16] the constants are blended with a function of the form $F_1 = tanh(x^4)$. We decide to use F_2 to blend the constants, because F_2 yields a smoother transition between RANS and LES. To evaluate the effect of this modification in the RANS model, we performed RANS simulations (not presented) of the flow around an airfoil at an angle of attack of 13^o. The results did not show any significant differences.

2. *LES k^{sgs} one-equation model*

$$\frac{\partial}{\partial t}(\bar{\rho}k^{sgs}) + \frac{\partial}{\partial x_j}(\bar{\rho}\widetilde{u}_j k^{sgs}) = \frac{\partial}{\partial x_j}\Big[(\frac{\widetilde{\mu}}{Pr} + \frac{\mu_{sgs}}{Pr_t})\frac{\partial k}{\partial x_j}\Big] + \tau_{ij}^{sgs}\frac{\partial \widetilde{u}_i}{\partial x_j} - C_\varepsilon\rho\frac{(k^{sgs})^{3/2}}{\Delta} \tag{17}$$

$$\begin{aligned}\mu_{sgs} = \overline{\rho}C_\nu\Delta\sqrt{k^{sgs}}, \quad C_\nu = 0.0667, \quad C_\varepsilon = 0.916, \quad Pr = 0.72, \\ Pr_T = 0.9, \quad \Delta = (\Delta x\Delta y\Delta z)^{1/3}, \quad \widehat{\Delta} = 2\Delta\end{aligned} \tag{18}$$

For 3D flows, a dynamic approach is implemented to obtain appropriate values for the coefficients C_ν and C_ε. Here, it is assumed that the subgrid stress tensor and the subgrid scale dissipation satisfy the similarity assumption in both grid and test filters (Menon[18]). Equations (19-20) define the subgrid stress tensor and subgrid energy dissipation with their respective closure form:

$$-\tau_{ij}^{sgs} = \bar{\rho}\big(\widetilde{u_i u_j} - \widetilde{u}_i\widetilde{u}_j\big) = -2\frac{C_\nu\Delta}{\overline{\rho}}\Big(\frac{1}{2}\widetilde{u_i u_i} - \frac{1}{2}\widetilde{u}_i\widetilde{u}_i\Big)^{1/2}\Big(\widetilde{S}_{ij} - \frac{1}{3}\widetilde{S}_{kk}\delta_{ij}\Big) + \frac{2}{3}\bar{\rho}\Big(\frac{1}{2}\widetilde{u_i u_i} - \frac{1}{2}\widetilde{u}_i\widetilde{u}_i\Big)\delta_{ij} \tag{19}$$

$$Diss = \widetilde{\tau_{ij}\frac{\partial u_i}{\partial x_j}} - \widetilde{\tau}_{ij}\frac{\partial\widetilde{u}_i}{\partial x_j} = \overline{\rho}C_\varepsilon\frac{\Big(\frac{1}{2}\widetilde{u_i u_i} - \frac{1}{2}\widetilde{u}_i\widetilde{u}_i\Big)^{3/2}}{\Delta} \tag{20}$$

where, $\widetilde{S}_{ij} = \frac{1}{2}\big(\frac{\partial\widetilde{u}_i}{\partial x_j} + \frac{\partial\widetilde{u}_j}{\partial x_i}\big)$. If the similarity assumption holds, direct evaluation of equations (19-20) is possible in a coarser grid by means of a test filter $G'(r,x)$. Consequently, it is possible to calculate appropriate coefficients for the LES closure models with Eqs. (21-23). More details of LDKM have been reported elsewhere.[20]

$$C_\nu = -\frac{L_{ij}D_{ij}}{2D_{ij}D_{ij}} \tag{21}$$

$$\begin{aligned} L_{ij} &= \widehat{\bar{\rho}}\big(\widehat{\widetilde{u}_i\widetilde{u}_j} - \widehat{\widetilde{u}}_i\widehat{\widetilde{u}}_j\big) - \frac{\widehat{\bar{\rho}}}{3}\big(\widehat{\widetilde{u}_i\widetilde{u}_i} - \widehat{\widetilde{u}}_i\widehat{\widetilde{u}}_i\big)\delta_{ij}, \\ D_{ij} &= -\widehat{\Delta}\widehat{\bar{\rho}}\big(\frac{1}{2}\widehat{\widetilde{u}_i\widetilde{u}_i} - \frac{1}{2}\widehat{\widetilde{u}}_i\widehat{\widetilde{u}}_i\big)^{1/2}\big(\widehat{\widetilde{S}}_{ij} - \frac{1}{3}\widehat{\widetilde{S}}_{kk}\delta_{ij}\big) \end{aligned} \tag{22}$$

$$C_\varepsilon = 2\widehat{\Delta}(\widehat{\widetilde{\mu}+\mu_T})\frac{\Big[\overline{(\widetilde{S}_{ij} - \frac{1}{3}\widetilde{S}_{kk}\delta_{ij})\frac{\partial\widetilde{u}_i}{\partial x_j}} - (\widehat{\widetilde{S}}_{ij} - \frac{1}{3}\widehat{\widetilde{S}}_{kk}\delta_{ij})\frac{\partial\widehat{\widetilde{u}}_i}{\partial x_j}\Big]}{\widehat{\bar{\rho}}\Big(\frac{1}{2}\widehat{\widetilde{u}_i\widetilde{u}_i} - \frac{1}{2}\widehat{\widetilde{u}}_i\widehat{\widetilde{u}}_i\Big)^{2/3}} \tag{23}$$

$$\widehat{\widetilde{\phi}}_{sgs} = \frac{\int\overline{\rho}(x-r,t)\widetilde{\phi}(x-r,t)G'(r,x)dr}{\int\overline{\rho}(x-r,t)G'(r,x)}dr \tag{24}$$

C. HRLES Closures Terms

To finalize the HRLES formulation, Eq.(8), the turbulence transport and source terms in Eq. (9) must be defined. Here, only the momentum, total energy and "k" equation are considered. For the sake of simplicity, only the closure terms are included. The original unclosed terms can be found elsewhere.[21]

- Momentum closure:

$$\begin{aligned} \tau_{ij}^{rans} &= \mu_T\Big(\frac{\partial\widetilde{u}_i}{\partial x_j} + \frac{\partial\widetilde{u}_j}{\partial x_i} - \frac{2}{3}\frac{\partial\widetilde{u}_k}{\partial x_k}\delta_{ij}\Big) - \frac{2}{3}\overline{\rho}k\delta_{ij}, \\ \tau_{ij}^{sgs} &= \mu_{sgs}\Big(\frac{\partial\widetilde{u}_i}{\partial x_j} + \frac{\partial\widetilde{u}_j}{\partial x_i} - \frac{2}{3}\frac{\partial\widetilde{u}_k}{\partial x_k}\delta_{ij}\Big) - \frac{2}{3}\overline{\rho}k^{sgs}\delta_{ij} \end{aligned} \tag{25}$$

- Total energy closure:

$$\begin{aligned} E_j^{rans} &= (\widetilde{\mu} + \sigma_k\mu_T)\frac{\partial k}{\partial x_j} + \frac{C_p\mu_T}{Pr_T}\frac{\partial\widetilde{T}}{\partial x_j} + \widetilde{u}_i\tau_{ij}^{rans}, \\ E_j^{sgs} &= \frac{\mu_{sgs}}{Pr_T}\frac{\partial\widetilde{E}}{\partial x_j} + \frac{\mu_{sgs}}{\overline{\rho}Pr_T}\frac{\partial\overline{p}}{\partial x_j} + \frac{C_p\mu_{sgs}}{Pr_T}\frac{\partial\widetilde{T}}{\partial x_j} + \widetilde{u}_i\tau_{ij}^{sgs} \end{aligned} \tag{26}$$

- Turbulence "k" equation closure:

$$\begin{aligned} K_{j\ trans}^{rans} &= (\widetilde{\mu} + \sigma_k\mu_T)\frac{\partial k}{\partial x_j}, \quad K_{j\ trans}^{sgs} = (\frac{\widetilde{\mu}}{Pr} + \frac{\mu_{sgs}}{Pr_T})\frac{\partial k^{sgs}}{\partial x_j}, \\ K_{src}^{rans} &= \tau_{ij}^{rans}\frac{\partial\widetilde{u}_i}{\partial x_j} - \beta^*\overline{\rho}k\omega, \quad K_{src}^{sgs} = \tau_{ij}^{sgs}\frac{\partial\widetilde{u}_i}{\partial x_j} - C_\varepsilon\overline{\rho}\frac{(k^{sgs})^{3/2}}{\Delta} \end{aligned} \tag{27}$$

III. Numerical Method

The HRLES compressible Navier-Stokes equations (Eqs. (8-9)) are solved using a finite volume approach. Time integration is performed with a five stage Runge-Kutta dual time stepping scheme.[22] Convective fluxes are discretized with a second-order central scheme with numerical dissipation[23] to prevent spurious oscillations. Although high-order central schemes are desired for LES, it is not always easy to adapt those schemes on complex geometries. In fact, most of the previous LES simulations in airfoils have been obtained by second-order central schemes (see, for example, Refs. 2, 3, 24).

Boundary conditions are implemented explicitly. On the solid surface, the velocity is either zero for the static case or equal to the wing velocity for the unsteady motion. The wall is assumed adiabatic for the unsteady and static cases. Pressure and density are computed from interior points with first order extrapolation. For the unsteady motion, pressure is computed solving the normal momentum equation at the surface:

$$\frac{\partial p}{\partial n} = -\rho \widehat{n} \cdot a \tag{28}$$

where $\widehat{n}$ is the unit normal vector to the surface and a is the acceleration vector of the airfoil. Farfield boundary conditions are implemented by solving one-dimensional Riemann invariants. Periodic boundary conditions are applied for the boundaries in the spanwise direction. For the turbulence variables, the following holds: The modeled kinetic energy k is set to zero at the surface and to $k_\infty = (0.016 U_\infty)^2$ at the farfield. The specific dissipation rate (ω) is computed at the farfield from the scaling proposed in Ref. 25. At the wall, ω has an analytic solution described in Ref. 26. Nevertheless, for the current simulation, this solution is only imposed at the first finite volume cell neighboring the wall. These boundary conditions are:

$$\omega_\infty = \vartheta\Big(10\frac{U_\infty}{C}\Big), \qquad \omega = \frac{6\nu}{\beta_1 y_1^2} \quad \text{for} \quad y_1^+ < 2.5 \tag{29}$$

Here, C is the chord of the airfoil, ν kinematic viscosity, y_1 is the wall normal distance to the first finite volume cell center next to the wall, $y_1^+ = \frac{y_1}{\nu}\sqrt{\frac{\tau_w}{\rho}}$, and τ_w is the shear stress at the wall.

IV. Results and Discussion

The principal objective of the present investigation is to assess the capability of HRLES as a reliable tool to predict complex aerodynamic flows. To this end, the flow over static and oscillating airfoil were selected given the challenges that these flows pose to current turbulence models. The tripped boundary layer experimental data of Ref. 1 is used to compare the numerical calculations.

A. Experimental Description

The cases considered include the flow over a static and oscillating airfoil NACA 0015, at a Reynolds number based on the chord length $Re = 1.95 \times 10^6$ and Mach number $M = 0.29$. For the static case, angles of attack in the linear and stall regime were considered. For the oscillating airfoil, the angle of attack changes sinusoidally as $\alpha = \alpha_0 + \alpha_a \sin(\frac{2U_\infty \kappa}{C} t)$. Here, α_0 is the mean angle of attack, α_a is the amplitude of pitch, and κ is the reduced frequency. Three cases were selected: attached flow ($\alpha_0 = 4^o$, $\alpha_a = 4.2^o$, $\kappa = 0.1$), light stall ($\alpha_0 = 10.88^o$, $\alpha_a = 4.22^o$, $\kappa = 0.1$), and deep stall ($\alpha_0 = 13.03^o$, $\alpha_a = 5.25^o$, $\kappa = 0.1$). For further details about the experimental setup, refer to the original report in Ref. 1.

B. Numerical Configuration

Three-dimensional computation have been conducted on a C grid with $541 \times 97 \times 21$ grid points in the streamwise, wall normal, and spanwise directions, respectively. The wall normal and spanwise resolution are $y/C = 1.0 \times 10^{-5}$ and $z/C = 0.002$ which provide an approximate resolutions in wall units of $\Delta y^+ \approx 2.0$ in the normal and $\Delta z^+ \approx 200$ in the spanwise direction. For the 2D simulations, the same grid was implemented but with just one plane in the spanwise direction. Outer boundaries are set at approximately 8 chord distances.

C. Static 2D Simulations

The fact that a good turbulence model should provide accurate solutions at a minimum cost usually requires simplifications on the original problem. If three-dimensional effects can be neglected, 2D HRLES simulations can be performed without compromising the fidelity or physics of the results.

1. Attached flow regime

In a static semi-infinite wing, the attached flow is fundamentally two-dimensional. Therefore, 2D simulations can be performed to save computer time without loosing much information. Figure 1 presents the steady state aerodynamic coefficients at different angles of attack, including stall. For angles of attack before stall ($\alpha < 14^o$), 2D solutions reproduce loads in excellent agreement with experimental measurements. In the experiments, the aerodynamic coefficients were computed from pressure distributions only. The fact that the integrated aerodynamic coefficients match experiments does not always ensure an agreement in pressure distribution. Figure 2(a) presents Cp distribution extracted from 2D simulation at the onset of stall ($\alpha = 13^o$). The excellent agreement of the loads is determined by a corresponding accurate prediction in the pressure distribution. Therefore, for two-dimensional attached aerodynamic flows, 2D simulations suffice to reproduce results in agreement with experiments.

2. Stalled flow regime

For angles of attack in the stalled regime ($\alpha > 14^o$), flow separation is expected and turbulence structures cannot be accurately resolved by 2D HRLES simulations. Full 3D solution is needed, and its results are shown in Fig. 1 but also discussed further in the next section. In Fig. 1, 2D simulations overpredict the aerodynamic loads at high angles of attack due to unphysical prediction of flow separation. To illustrate this fact, Fig. 2(c) presents time averaged streamlines at $\alpha = 18^o$. In general, the flow develops a larger clockwise recirculation region than its 3D counterpart shown in Fig. 3(b). This larger separation is the cause of the overshoot in the drag and moment coefficients of 2D simulations. The strong separation can be explained by analyzing both streamlines patterns. In the 2D case, the lack of a third dimension generates a strong trailing edge vortex. This vortex pushes upstream the recirculation zone, increasing the separated region. For the 3D solution, this vortex is not as strong as its 2D counterpart is. Therefore, the recirculation region is smaller, and the location of the vortex is at the end of the trailing edge.

D. Static 3D Simulations

The stalled flow over a wing at angles of attack of $\alpha = 17^o$ and 18^o were simulated solving the full 3D equations. The aerodynamic coefficients were found in good agreement with experiments as shown in Fig. 1. However, the lift coefficient experienced a small over prediction caused by an approximate 30% overshoot of the mean Cp in the suction zone (Fig. 2(b)). This overshoot may be caused by the small wingspan simulated here. Nevertheless, away from this small zone, the pressure distribution is in good agreement with experiments. The recirculation zone, identified by the region of constant Cp in the suction side, is resolved correctly, it covers the approximate range of $x/C = 0.3 - 1.0$, for $\alpha = 17^o$. Drag and moment coefficients are not severely affected by the overshoot in Cp on the suction zone. In fact, the accuracy in drag prediction depends on an accurate match of the recirculation zone [c].

Unsteady flow features at $\alpha = 18^o$ are presented in Figure 3. Instantaneous streamlines shown in Fig. 3(a) reveal the complex flow structures encountered in the stalled wake. This wake consists of two principal structures. At the leading edge, after the flow separates a shear layer of high vorticity, reminiscent of a Kelvin-Helmholtz instability, develops covering a region of approximately half chord before it starts periodic vortex shedding. At the trailing edge a vortex periodically develops and convects downstream. The fact that the flow is asymmetric ensures that the natural frequencies of these structures are not in phase. Contrary to the harmonic vortex shedding in a cylinder, for the stalled airfoil the clockwise leading edge vortex directly interacts with the anticlockwise trailing edge vortex. This complex vortex dynamics breaks large-scale vorticity into small eddies, continuously developing new turbulence scales that sustain the turbulence levels in the flow.

[c] This is only valid for loads computed directly from pressure distribution.

Figure 3(c) presents contours of instantaneous vorticity. Here, it is evident that the small eddies are mainly localized near the trailing edge zone. These eddies are generated by the interaction of the leading and trailing edge vortices (also visualized in the figure). Therefore, in this region, we expect the highest levels of turbulence intensities.

Here, we demonstrate that these unsteady flow features are captured by the LES part of the HRLES model. Contours of instantaneous values of the blending function (Eq. 15), are presented in Fig. 3(d). It is evident that in the leeward side of the airfoil, where unsteady flow features are observed, transition from RANS to LES occurs faster than in the windward side, where a slower transition is reproduced, mainly by the absence of enough flow unsteadiness. The fast leeward RANS to LES transition is caused by the change in the definition of the "k" in Eq. (15). In the original RANS-SST, "k" represents the complete turbulent kinetic energy. However, "k^{sgs}" represents only a small fraction of this energy in LES. Therefore, in HRLES the transition function switches faster than it would normally do in a standard RANS simulation.

Spectral analysis are performed on time sampled data of velocity components. Data were collected at two locations as summarized in Table 1 and Fig 4. These locations were selected to capture the vortex structures in the trailing and leading edge, after analyzing the flow evolution. For $\alpha = 18^o$, the trailing edge vortex shedding frequency is computed from the vorticity spectrum and shown in Fig 5(a). A primary frequency of 321 Hz with a Strouhal number of $St = fC/U_\infty = 0.96$ is identified. Additionally, a second frequency at around half the value of the primary frequency and a third frequency at exactly twice the value of the primary frequency are also observed. In Ref. 3, frequencies corresponding to $St \sim 1.3$ were reported for $\alpha = 13^o$.

Figure 5(b) presents the energy spectrum of the turbulence. Here, it is observed that most of the energy is contained between 101.5 Hz and 321.3 Hz. From Fig. 5(a) these frequencies are identified as the vortex shedding frequencies. Therefore, vortex shedding is recognized as the principal large-scale mechanism feeding energy into viscous dissipation. In addition, an inertial range following Kolmolgorov[27] scaling is reproduced. Finally, Fig. 6 presents the contours of the resolved Reynolds stresses for $\alpha = 18^o$. The shear layer and trailing edge zones show higher levels of $< u'u' >$ (Fig. 6(a)). However, only at the trailing edge $< v'v' >$ is found in reasonable levels (Fig. 6(b)). From Figs. 5(b) and 6(d), it is evident that the trailing edge region produces the highest turbulence activity in the flow.

Table 1. Probe locations.

Location	x/C	y^*/C	z/C
1	1.0	6.0×10^{-2}	0.02
2	0.3	3.0×10^{-2}	0.02

* Distance measured from the airfoil surface.

E. Oscillating Flow 2D and 3D Simulations

For all the cases simulated, the same reduced frequency of $\kappa = 0.1$ is used. The flow is initialized from a steady state solution at the lowest angle of attack, the first transitory cycle is eliminated, and an approximate time step of $\Delta t \approx 4.0 \times 10^{-6}$s is used to advance the solution.

1. Attached flow (2D)

The pitching case of $\alpha = 4^o + 4.2^o \sin(\omega t)$ results in attached flow. Even though separation is absent in this configuration, the growth of the boundary layer imposes enough complexity for the turbulence model. Figure 7 shows the unsteady loads in this case. C_D shows a small underprediction during the cycle, whereas, C_L only underpredicts the experiment at the top of the upstroke. C_M shows good agreement in the downstroke, and a small over prediction at the upstroke. In general, the three aerodynamic coefficients are in good agreement with experimental data. Only three cycles were simulated since the third cycle was found to be identical to the second cycle.

2. Light stall (2D)

For this case, the angle of attack is $\alpha = 10.88^o + 4.22^o \sin(\omega t)$. In the experiments, only a small region of separation occurs at the end of the upstroke. Therefore, 2D simulations may still provide reasonable solutions. Figure 8 shows the aerodynamic loads for each cycle and their cycle average. Here, six cycles were simulated and cycle-to-cycle variations were observed. The flow exhibits a small trailing edge separation and vortex shedding. It starts at the end of the upstroke and persists up to halfway of the downstroke. Lift coefficient recovers faster during the downstroke, and higher C_L levels are seen in Fig. 8(a). This higher recovery is also found in previous RANS-SST simulations (see Ref. 11). Drag coefficient shown in Fig. 8(b) is found in fair agreement with the experiment. The upstroke is well predicted until the onset of stall, where suddenly the C_D increases. During the first part of the downstroke, the drag induced by the separation is well captured. However, a faster recovery in the drag is experienced when the flow reattaches. The pitching moment coefficient shown in Fig. 8(c) exhibits high frequency oscillations caused by vortex shedding in the downstroke for $15.1^o > \alpha > 11^o$. Similar behavior is also apparent for C_L and C_D, although to a smaller extent. It is evident that the separation affects C_M down to approximately $\alpha \approx 11^o$ in the downstroke at which time the flow completely reattaches. In addition, C_M cycles exhibit a loop crossing, like those found in cases with higher amplitude of pitch, mainly during the end of the upstroke and the beginning of the downstroke. The rest of the cycle in Fig. 8 shows faster recovery in the loads (compared with experiments), as also reported in other studies (Ref. 11). It appears that for the attached and light stall cases, RANS-SST model dominates a majority of the HRLES solution. In addition, it is observed that the excessive 2D separation will induce apparent higher amplitude of pitch responsible of the loop crossing shown in the computed moment coefficient.

F. Oscillating Wing 3D Simulations

It was shown in Fig. 1 that three-dimensional effects cannot be neglected when flow separation is encountered. Therefore, even for light stall cases 3D simulations are required for accurate predictions. Here, a more challenging, fully stalled case with $\alpha = 13.03^o + 5.25^o \sin(\omega t)$ is simulated in 3D. In addition, 2D simulations were conducted for comparison purposes.

1. Deep stall results (2D)

Figure 10 presents the aerodynamic loads for the deep stall case. Each cycle (after the first cycle) as well as the cycle average are presented. The cycle average was computed from nine cycles, all of them were found to have unique cycle-to-cycle variation in the solution. This number of cycles may not be enough to get a smooth converged mean cycle, since in the experiments of Ref. 1, over twenty cycles were required to get a converged mean. Nevertheless, the current mean results help to exemplify the possible problems encountered when unsteady HRLES or LES solutions of dynamic stall have to be compared against classic cycle-averaged experimental data[d]. Therefore, we limit ourselves to describe only the characteristics of individual cycles.

During the upstroke, the three coefficients showed very good agreement with experimental data. Here, the characteristic delay in stall is well captured. However, at the end of the upstroke and during most of the downstroke, excessive unphysical 2D separation induces an overshoot in the loads. This is characterized by high frequency, high amplitude oscillation. In the light stall case, vortex shedding at the trailing edge caused a high frequency, small amplitude oscillation in the loads. Nonetheless, for the deep stall case, vorticity is shed from the leading and trailing edge. The strong oscillations encountered in the loads are produced by a complex interaction between the leading edge vortex or "dynamic stall vortex" and the trailing edge vortex. Because the flow is 2D, these vortices are too strong with low-pressure cores. Therefore, they continuously change the pressure distribution of the airfoil on its way through the wake. Figure 9 presents snapshots of the evolution of one cycle. Contours of vorticity magnitude are used to demonstrate the complex structure of this flow. During the upstroke, the unsteady effects keep the flow attached well above the steady state stall limit ($\alpha > 14^o$), and even at $\alpha = 18^o$ the stall is still light when compared with the static case. Additionally, a clockwise leading edge vortex is formed (dynamic stall vortex) and this vortex is responsible for the dramatic increase in lift. Once the airfoil starts the downstroke motion, the dynamic stall vortex separates from the leading edge convecting through the wake. At the same time, a counterclockwise vortex is generated at the trailing edge. Both vortices usually are not in phase. Thus, a complex vortex dynamics occurs when both

[d]Usually, experiments in dynamic stall mainly report the aerodynamic loads as cycle-averaged data.

vortices, of opposite signs, collide in the leeward side of the airfoil. This complex interaction is responsible for the oscillations in the loads. On an average, the flow reattaches around $\alpha = 12^o$, and the cycle starts over again.

2. Deep stall results (3D)

Given current limitations in computational resources, only one cycle has been simulated so far (simulations will be continued in the future). For this case computations were initiated from the steady state solution at $\alpha = 18^o$ and the initial transient is eliminated by the time the airfoil reaches the bottom of the downstroke. Figure 11 presents the unsteady aerodynamic loads for the 3D simulation (2D results are also included as a reference). It is evident that the effect of the third dimension is to reduce the intensity of separation. The frequency and amplitude of the oscillations in the loads is dramatically reduced when compared with 2D results. During the upstroke, lift, drag, and pitching moment coefficients show very good agreement with the experiments. Contrary to the 2D solution, the 3D simulation correctly predicts the load at the end of the upstroke where an overshoot is present in the 2D result. Similar to the 2D case, a dynamic stall and a trailing edge vortex form during the downstroke. However, these vortices are not as strong as their 2D counterpart. Therefore, the fluctuations in the loads are not very intense. Nevertheless, in the range $\alpha \approx 17^o \rightarrow 15^o$ the loads present an over-prediction. However, in the original experimental report (Ref. 1) individual cycles for a similar case presented important overshoots of the loads, when compared with mean values. As explained before, the complex interaction between these two vortices is responsible for the oscillation in the loads. The current 3D simulation correctly predicts the angle at which the drag and the pitching moment loops crosses ($\alpha \approx 14^o$). Additionally, 3D loop is closer to the experimental data than the mean 2D loop. Based on these results, we believe that if enough 3D cycles are simulated, the mean loop would be closer to the experiments. Figures 12 and 13 present snapshots of the time evolution of the cycle, in terms of contours of vorticity magnitude (shown at the same level as in Fig. 10) and vorticity magnitude isosurfaces. Even though, Figs. 10 and 12 give the impression of similar flow dynamics, it is clear from Fig. 13 that this is not the case. During the upstroke, at the onset of stall, a two-dimensional wake develops as shown in Fig. 14(a). This 2D wake is unstable and spanwise instabilities trigger transition from 2D to 3D flow (Fig. 14(b)). From Figs. 14(c)- 14(e) it can be identified that vortex shedding induces an enlargement and division of the vortex structures. This mechanism, known as vortex stretching, redistributes vorticity in the three directions and enhance turbulence generation. The absence of vortex stretching in 2D prevents the 3D redistribution of vorticity, yielding unphysical levels of vorticity in the spanwise direction. Additionally, turbulence cannot be physically generated without vortex stretching. Finally, at the end of the downstroke the flow reattaches, recovering a 2D structure (Fig. 14(d)).

Power density spectra of the aerodynamic loads, vorticity magnitude and TKE are computed at locations 1 and 2. Figure 15(a) shows the power density spectra of the normalized vorticity magnitude and the aerodynamic coefficients. Vorticity magnitude is collected at location 2, where it is expected that the dynamic stall vortex would be located. It is clear that the spectrum of vorticity at this location is in agreement with the spectra of the aerodynamic loads. Figure 15(c) present the same spectra but at location 1. Here, the vorticity spectrum does not match the spectra of the aerodynamic loads. Additionally, Fig. 15(b) shows the time signal of drag coefficient and vorticity magnitude at location 1 and 2 during the downstroke. It can be observed, that the leading edge vortex signal shows a better phase agreement with the drag coefficient than the trailing edge vortex signal. These observations give the impression that the spectral characteristics of the aerodynamic coefficients are highly determined by the dynamic stall vortex. These would suggest that the leading edge must be as well resolved as the trailing edge in order to correctly predict the unsteady aerodynamic loads. Finally, Fig. 15(d) presents turbulence kinetic energy spectrum computed at location 1. Two principal frequencies containing most of the energy (140 Hz and 260 Hz) are identified. This spectrum presents an inertial range in agreement with Kolmolgorov's[27] scaling laws, indicating that the flow solution presents a distribution of energy in agreement with real turbulent flows. Previous RANS simulations for the same deep stall case (Ref. 28) have demonstrated that current RANS models still require more development to accurately simulate this flow. Consequently, HRLES emerges as a new and interesting alternative for dynamic stall simulations.

V. Conclusion

The performance of a new hybrid RANS-LES method is evaluated in flows of interest in aerodynamic designs. Two-dimensional and three-dimensional simulations for static and oscillating wings are carried out. Current results demonstrate that HRLES methods can provide accurate unsteady flow solutions, without the prohibitively high grid resolution required by LES. It is demonstrated that for flows that are inherently two-dimensional, and without flow separation, 2D HRLES simulation provides accurate solutions. However, when separation is present, only a three-dimensional simulation did yield solutions in agreement with experimental results. Additionally, proper domain dimensions have to be used to avoid additional separation caused by domain restriction. Here, it is suspected that the wingspan simulated is not big enough and is promoting additional (and unphysical) separation. This could explain the slight overshoot in the aerodynamic loads for the 3D deep stall case. These issues have to be explored further in future studies. It is very unlikely that standard LES models will be used in the near future as a design tool for complex industrial applied aerodynamic flows. Therefore, hybrid methods emerge as an interesting alternative for aerodynamic flows at high Reynolds number. Finally, future experimental measurements should provide unsteady flow characteristics in addition to typical mean values, to fully validate future unsteady simulations in dynamic stall.

VI. Acknowledgments

This work is sponsored by the National Rotorcraft Technology Center (NTRC) at the Georgia Institute of Technology. The computer resources of the Department of Defense Major Shared Resource Centers (MSRC) are gratefully acknowledged. The first author would also like to thank the National Council of Science and Technology of México (CONACYT) for the economic support provided.

References

[1]Piziali, R. A., "An experimental investigation of 2D and 3D oscillating wing aerodynamics for a range of angle of attack including stall." *NASA Technical Memorandum.*, 1993.

[2]Mary, I. and Sagaut, P., "Large Eddy Simulation of Flow Around an Airfoil Near Stall." *AIAA Journal.*, Vol. 40, No. 6, 1994, pp. 1139–1145.

[3]Mellen, C. P., Fröhlich, J., and Rodi, W., "Lessons from LESFOIL Project on Large-Eddy Simulation of Flow Around an Airfoil." *AIAA Journal.*, Vol. 41, No. 4, 2003, pp. 573–581.

[4]Speziale, C. G., "Turbulence Modeling for Time Dependent RANS and VLES: A review." *AIAA Journal.*, Vol. 36, No. 2, 1998, pp. 173–184.

[5]Spalart, P., Jou, W., Strelets, M., and Allmaras, S. R., "Comments on the feasibility of LES for wings and on a hybrid RANS/LES approach." *1st AFOSR Int. Conf. on DNS/LES, Aug. 4-8, 1997, Ruston, LA. In: Advances in DNS/LES, C. Liu and Z. Liu Eds., Greyden Press, Columbus, OH, USA*, 1997.

[6]Spalart, P. and Allmaras, S. R., "A One Equation Turbulence Model for Aerodynamic Flows," *La Recherche Aerospatiale*, Vol. 1, 1994, pp. 5–21.

[7]Xiao, X., Edwards, J. R., Hassan, H. A., and Baurle, R. A., "Inflow Boundary Conditions for Hybrid Large Eddy/Reynolds Averaged Navier-Stokes Simulations," *AIAA Journal.*, Vol. 41, No. 8, 2003, pp. 1481–1489.

[8]Xiao, X., Edwards, J. R., and Hassan, H. A., "Blending Functions in Hybrid Large-Eddy/Reynolds-Averaged Navier-Stokes Simulations." *AIAA Journal.*, Vol. 42, No. 12, 2004, pp. 2508–2515.

[9]Baurle, R. A., Tam, C. J., Edwards, J. R., and Hassan, H. A., "Hybrid Simulation Approach for Cavity Flows: Blending, Algorithm, and Boundary Treatment Issues." *AIAA Journal.*, Vol. 41, No. 8, 2003, pp. 1463–1480.

[10]Srinivasan, G. R., Ekaterinaris, J. A., and McCroskey, W. J., "Evaluation of Turbulence modes for unsteady flows of an oscillating airfoil." *Computers and Fluids*, Vol. 24, No. 7, 1995, pp. 833–861.

[11]Ekaterinaris, J. A. and Menter, F. R., "Computation of Oscillating Airfoil Flows with One and Two Equation Turbulence Models," *AIAA Journal.*, Vol. 32, No. 13, 1994, pp. 2259–2365.

[12]Ko, S. and McCroskey, W. J., "Computations of unsteady separating flows over an oscillating airfoil." *AIAA Journal.*, Vol. 35, No. 7, 1993, pp. 1235–1238.

[13]Ekaterinaris, J. A., "Numerical investigation of dynamic stall of an oscillating wing." *AIAA Journal.*, Vol. 33, No. 10, 1995, pp. 1803–1808.

[14]Ekaterinaris, J. A. and Platzer, M. F., "Computational prediction of airfoil dynamic stall," *Prog. Aerospace Sci.*, Vol. 33, 1997, pp. 759–846.

[15]Spentzos, S., Barakos, G., Badcock, K., Richards, B., Wernet, P., Schreck, S., and Raffel, M., "Investigation of Three-Dimensional dynamic stall using computational fluid dynamics." *AIAA Journal.*, Vol. 43, No. 5, 2005, pp. 1023–1033.

[16]Menter, F. R., "Two-equation eddy-viscosity turbulence models for engineering applications," *AIAA Journal.*, Vol. 32, No. 8, 1994, pp. 1598–1605.

[17]Menon, S. and Kim, W.-W., "A New Dynamic One-Equation Subgrid Model for Large-Eddy Simulations," *AIAA Paper No 95-0356*.

[18]Menon, S., Yeung, P. K., and Kim, W. W., "Effect of Subgrid Models on The Computed Intersacle Energy Transfer in Isotropic Turbulence," *Computers and Fluids*, Vol. 25, No. 2, 1996, pp. 165–180.

[19]Kim, W. W., Menon, S., and Mongia, H., "Large eddy simulations of a gas turbine combustor flow." *Combustion Science and Technology*, Vol. 143, 1999, pp. 25–62.

[20]Kim, W. W. and Menon, S., "A new incompressible solver for large-eddy simulations," *Int. Journal of Numerical Methods if Fluids.*, Vol. 31, 1999, pp. 983–1017.

[21]D.C.Wilcox, *Turbulence Modeling for CFD.*, CDW Industries 2nd ed., 1998.

[22]Jameson, A., "Time Dependent Calculations Using Multigrid, with Applications to Unsteady Flows Past Airfoils and Wings," *AIAA paper 91-1596*, 1991.

[23]Jameson, A., Schmidt, W., and Turkel, E., "Numerical solution of the Euler Equations by finite volume methods using Runge Kutta time stepping schemes," *AIAA paper 81-1259*, 1981.

[24]Davidson, L., Cokljat, D., Fröhlich, J., Leschziner, M. A., Mellen, C., and Rodi, W., *Lesfoil: Large Eddy Simulation of Flow Around a High Lift Airfoil.*, Springer., 2003.

[25]Menter, F. R., "Influence of Freestream Values on $k - \omega$ Turbulence Model Prediction," *AIAA Journal.*, Vol. 30, No. 6, 1992, pp. 1657–1659.

[26]Wilcox, D. C., "Reassessment of the Scale-Determining Equation for Advanced Turbulence Models," *AIAA Journal.*, Vol. 26, No. 11, 1988, pp. 1299–1310.

[27]Pope, S. B., *Turbulent Flows.*, Cambridge University Press., 2000.

[28]Shelton, A., Jennifer, A., Brandon, H., Sanchez-Rocha, M., Smith, M. J., and Menon., S., "An Investigation of the Numerical Prediction of Static and Dynamic Stall," *American Helicopter Society 61st Forum, Grapevine, TX, USA. June 1-3.*, 1995.

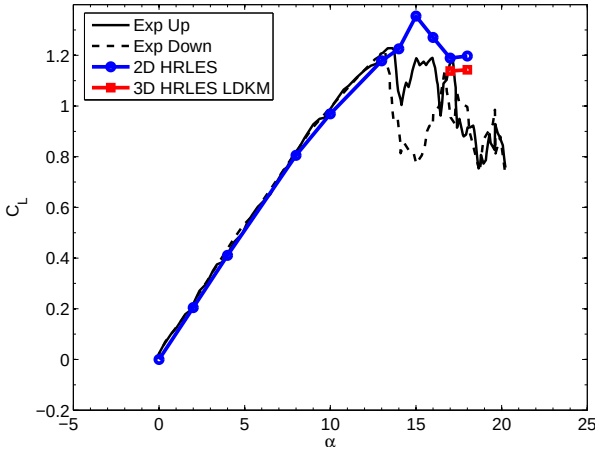

(a) Static lift coefficient.

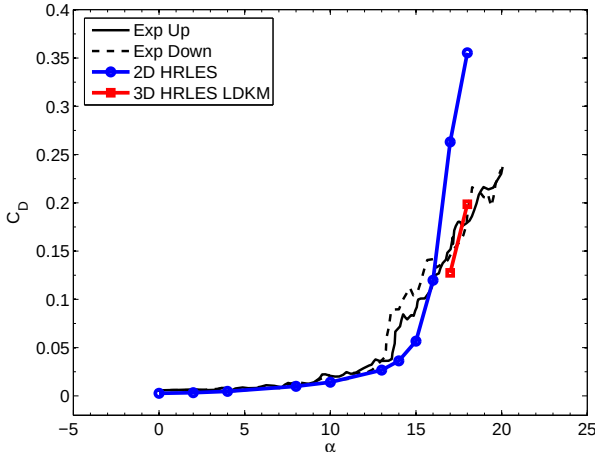

(b) Static drag coefficient.

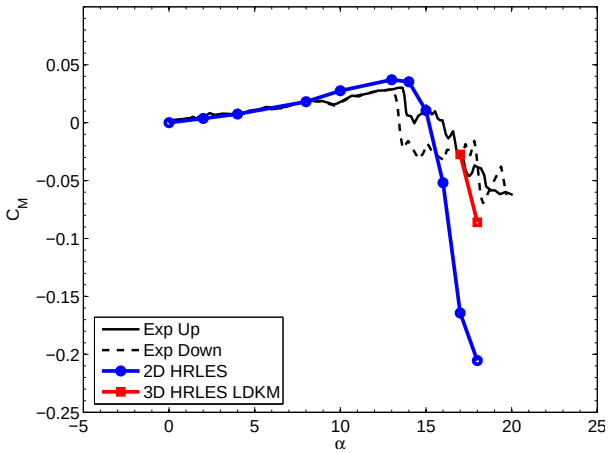

(c) Static moment coefficient.

Figure 1. Static lift, drag and moment coefficient for NACA 0015.

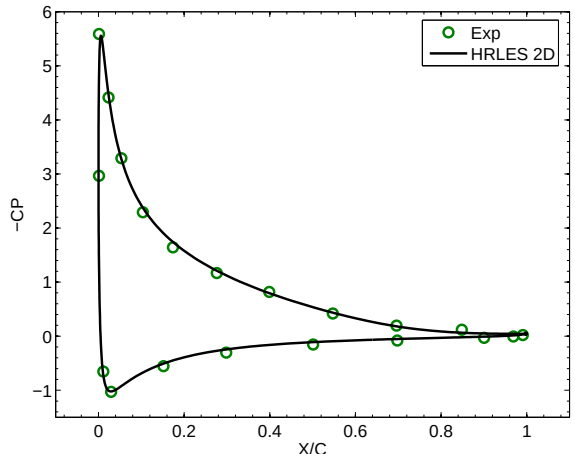

(a) Angle of attack $\alpha = 13^o$, 2D simulation.

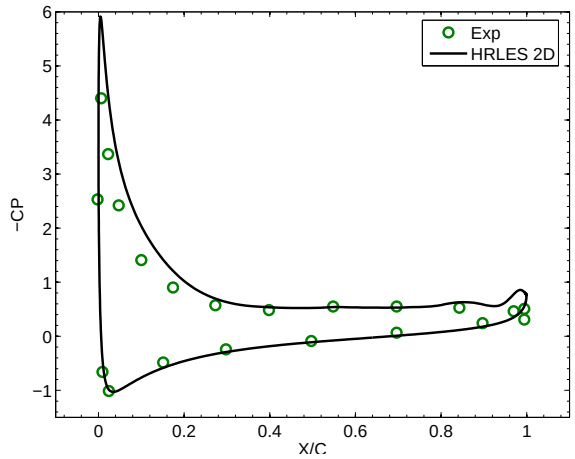

(b) Angle of attack $\alpha = 17^o$, 3D simulation.

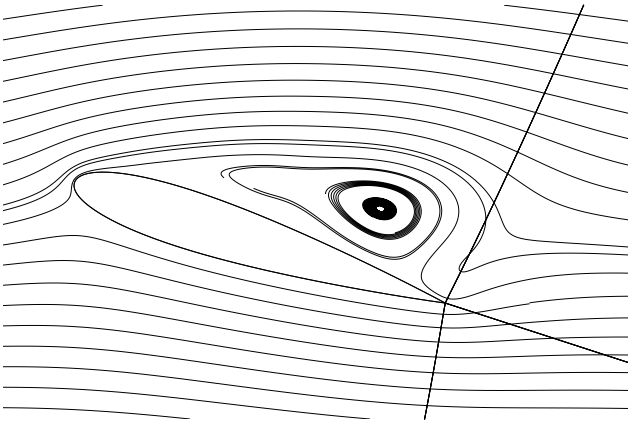

(c) Time average streamlines $\alpha = 18^o$, 2D simulation.

Figure 2. Pressure coefficient and time averaged streamlines for NACA 0015.

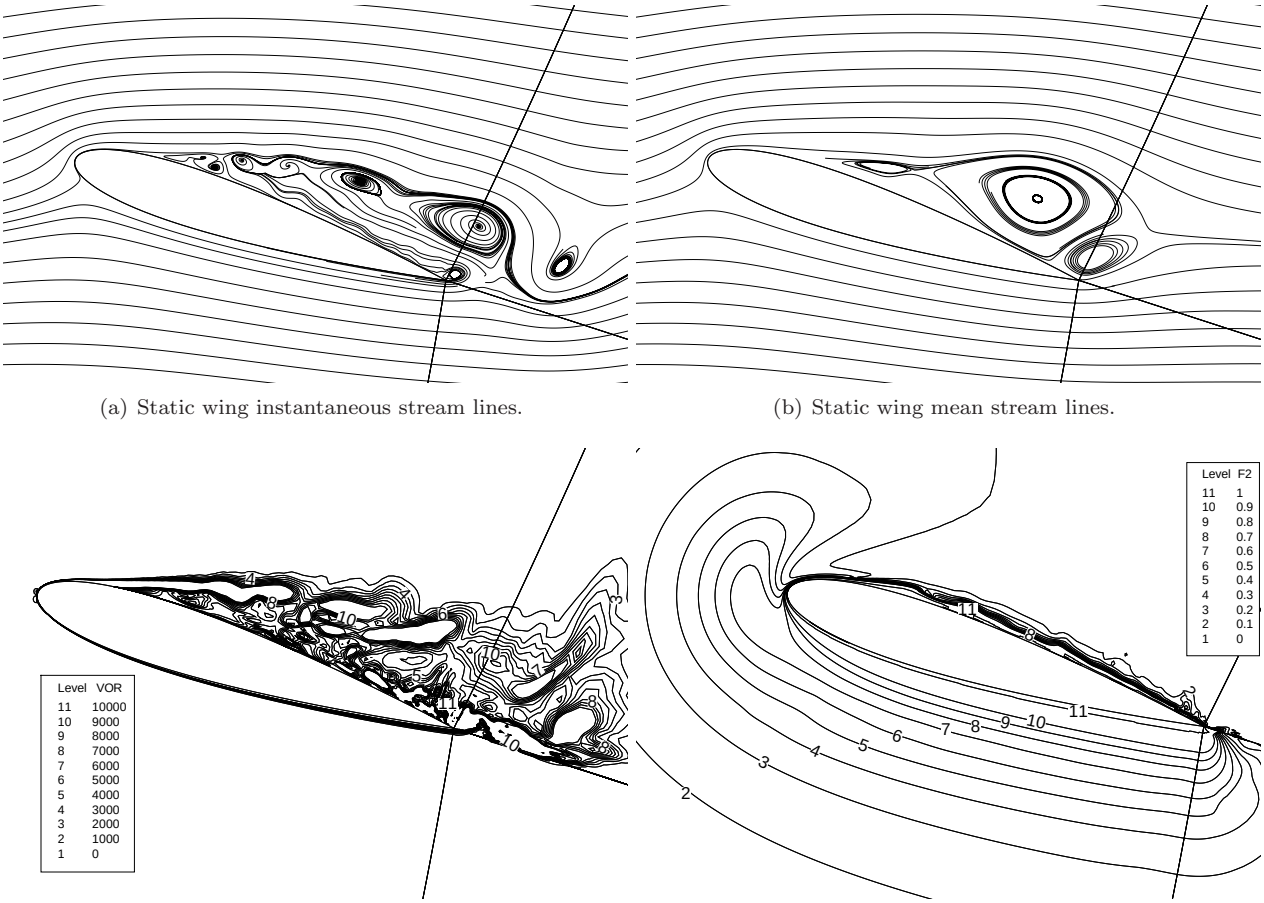

(a) Static wing instantaneous stream lines.

(b) Static wing mean stream lines.

(c) Static wing instantaneous vorticity magnitude contours.

(d) Static wing instantaneous F_2 blending function.

Figure 3. Mean and instantaneous streamlines, and contours of instantaneous vorticity and F_2 blending function. Static wing for NACA 0015.

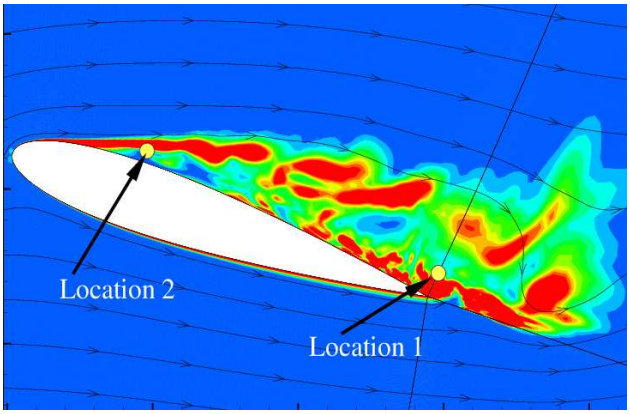

Figure 4. Probes locations for NACA 0015.

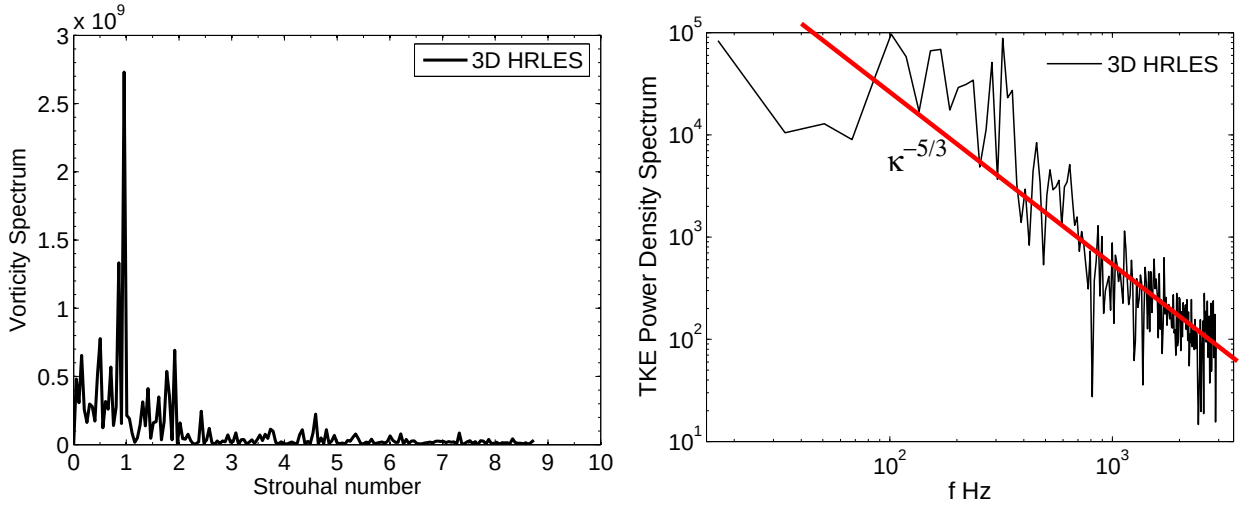

(a) Vorticity spectrum location 1.

(b) Energy spectrum location 1.

Figure 5. Power density spectrum of vorticity and turbulent kinetic energy at location 1. Static wing NACA 0015.

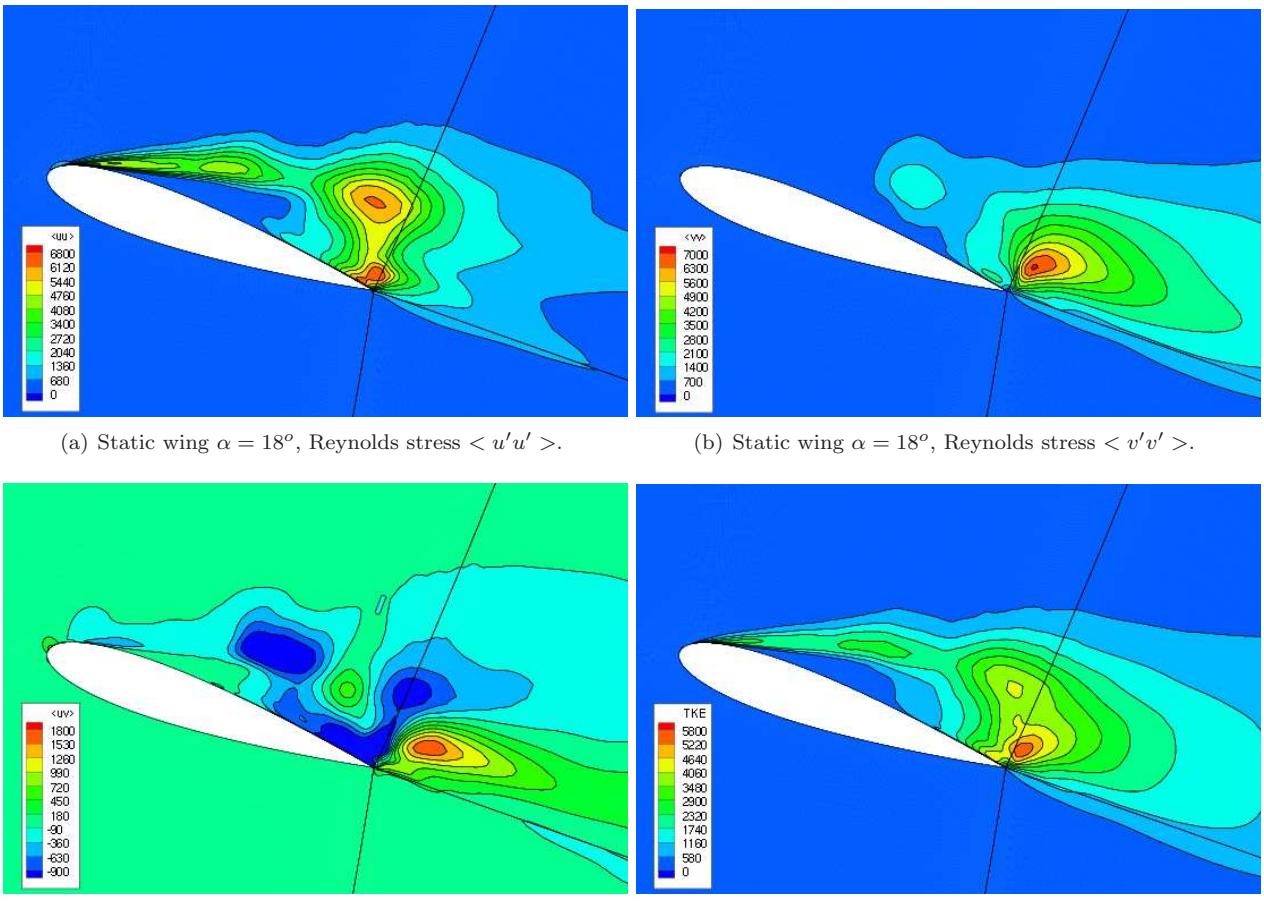

(a) Static wing $\alpha = 18^o$, Reynolds stress $< u'u' >$.

(b) Static wing $\alpha = 18^o$, Reynolds stress $< v'v' >$.

(c) Static wing $\alpha = 18^o$, Reynolds stress $< u'v' >$.

(d) Static wing $\alpha = 18^o$, TKE $< u_i'u_i' > /2$.

Figure 6. Contours of resolved Reynolds stresses and turbulent kinetic energy. Static wing NACA 0015.

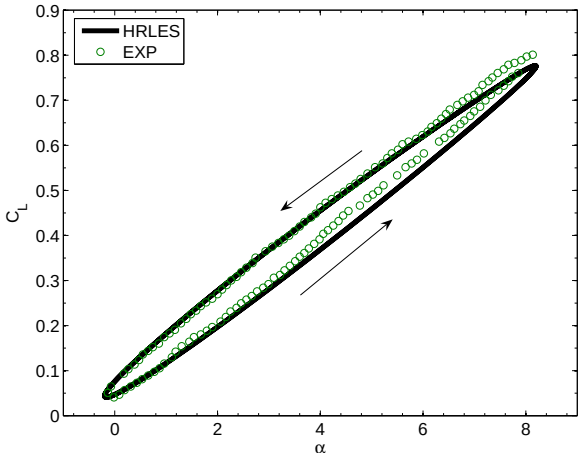

(a) Unsteady lift coefficient in oscillating motion.

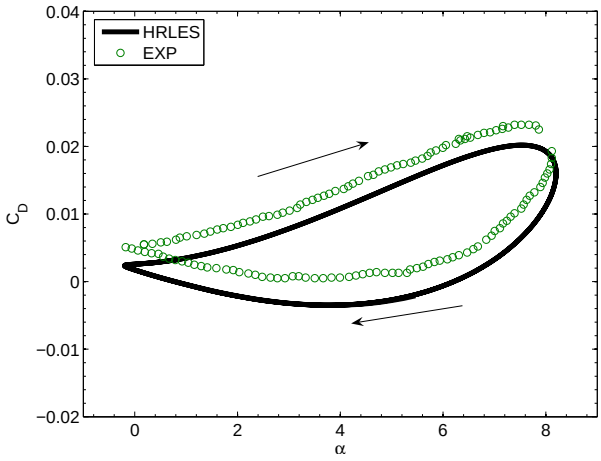

(b) Unsteady drag coefficient in oscillating motion.

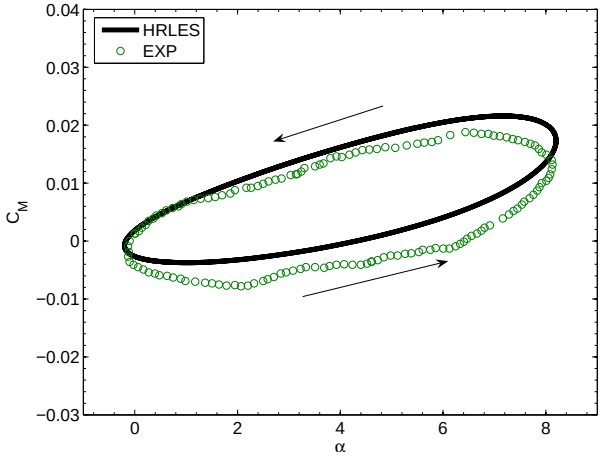

(c) Unsteady moment coefficient in oscillating motion.

Figure 7. Hysteresis of unsteady loads for attached flow. NACA 0015, $\alpha = 4 + 4.2\sin(\frac{2kU_\infty t}{C})$, $k = 0.1$, $M_\infty = 0.29$, $Re = 1.95 \times 10^6$, **2D results.**

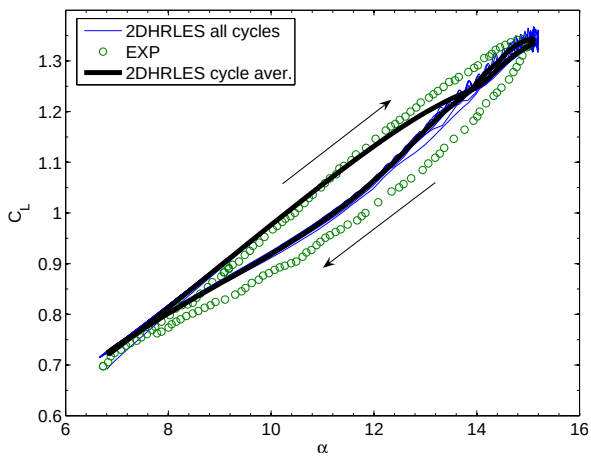

(a) Unsteady lift coefficient in oscillating motion.

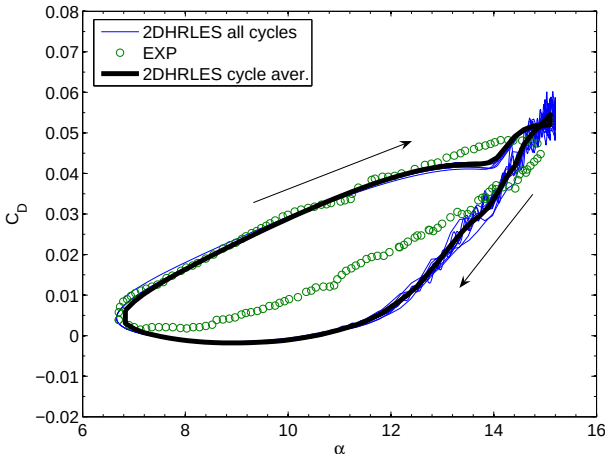

(b) Unsteady drag coefficient in oscillating motion.

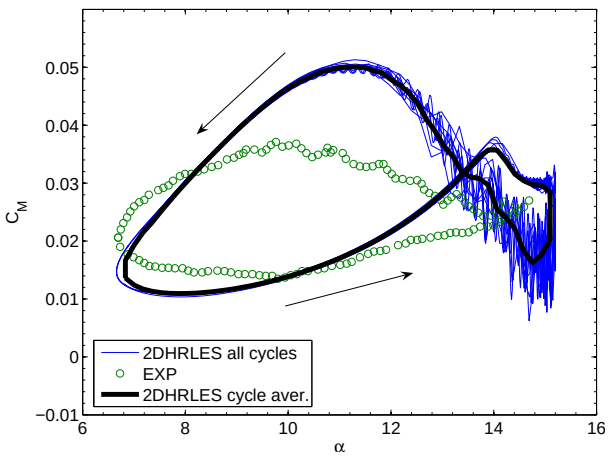

(c) Unsteady moment coefficient in oscillating motion.

Figure 8. Hysteresis of unsteady loads for light dynamic stall. NACA 0015, $\alpha = 10.88 + 4.22\sin(\frac{2kU_\infty t}{C})$, $k = 0.1$, $M_\infty = 0.29$, $Re = 1.95 \times 10^6$, **2D results.**

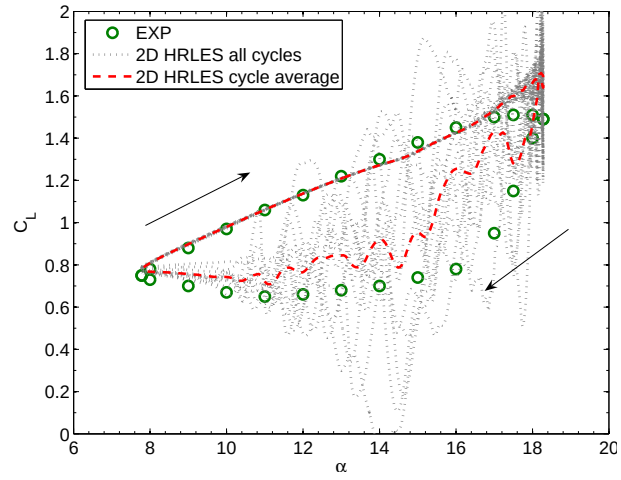

(a) Unsteady lift coefficient in oscillating motion.

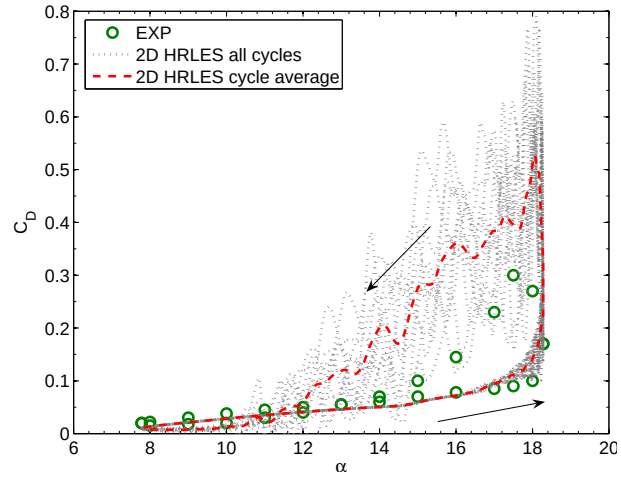

(b) Unsteady drag coefficient in oscillating motion.

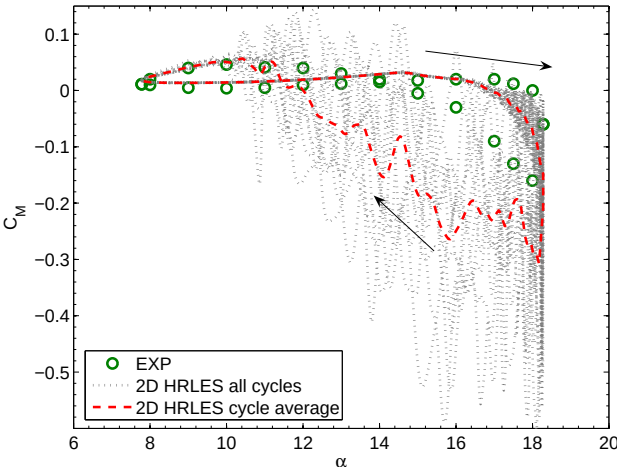

(c) Unsteady moment coefficient in oscillating motion.

Figure 9. Hysteresis of unsteady loads for deep dynamic stall. NACA 0015, $\alpha = 13.03 + 5.25\sin(\frac{2kU_\infty t}{C})$, $k = 0.1$, $M_\infty = 0.29$, $Re = 1.95 \times 10^6$, **2D results.**

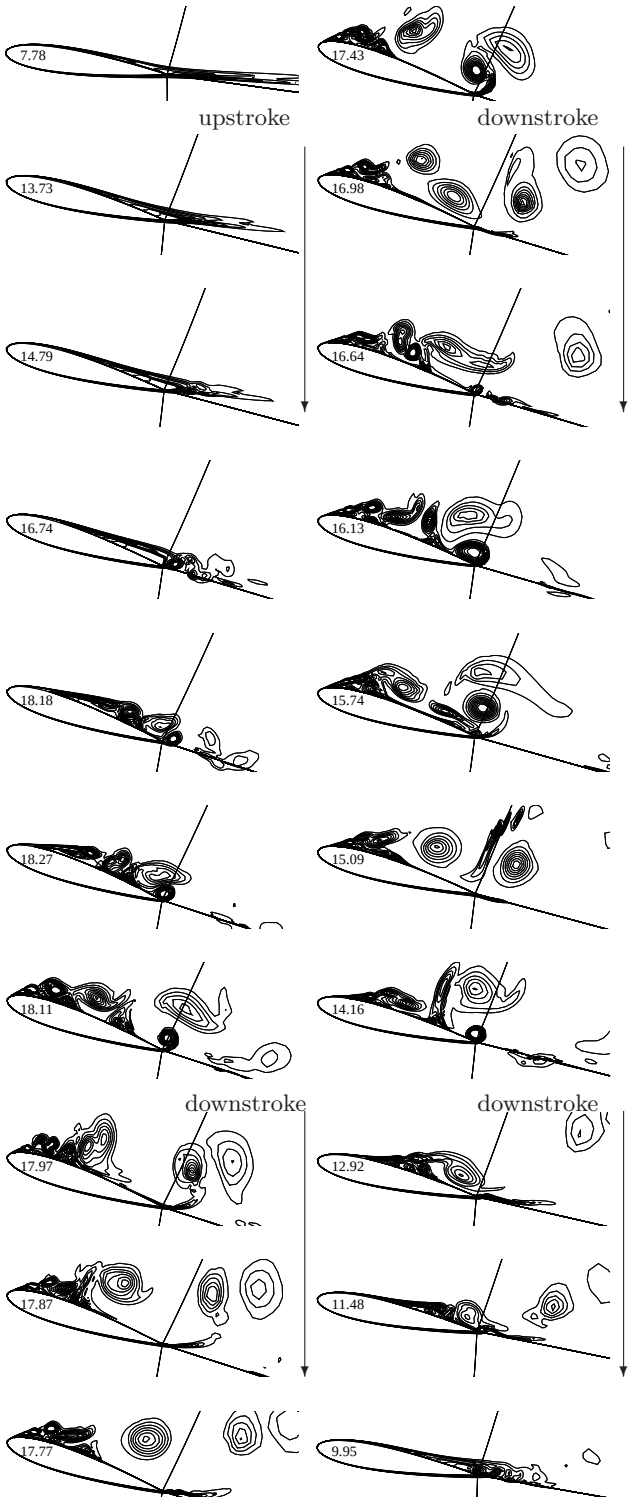

Figure 10. Instantaneous vorticity contours deep dynamic stall. NACA 0015, $\alpha = 13.03 + 5.25\sin(\frac{2kU_\infty t}{C})$, $k = 0.1$, $M_\infty = 0.29$, $Re = 1.95 \times 10^6$, **2D results.**

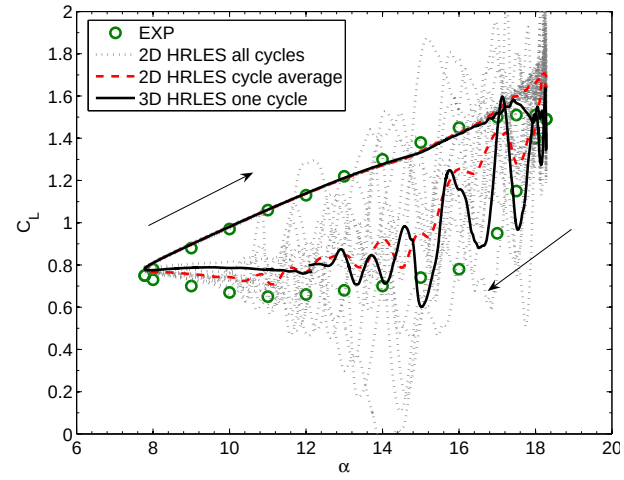

(a) Unsteady lift coefficient in oscillating motion.

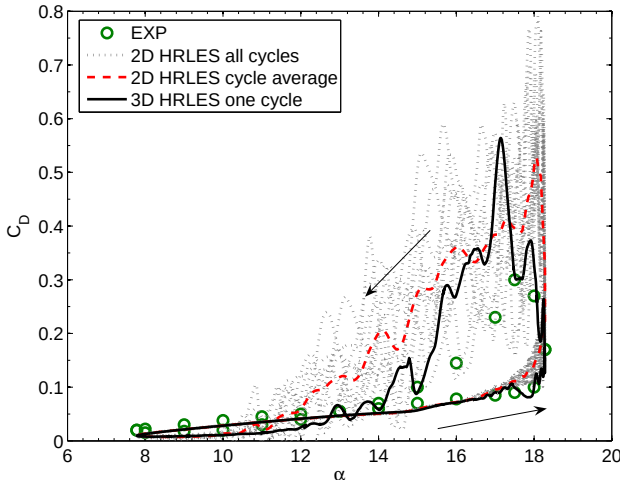

(b) Unsteady drag coefficient in oscillating motion.

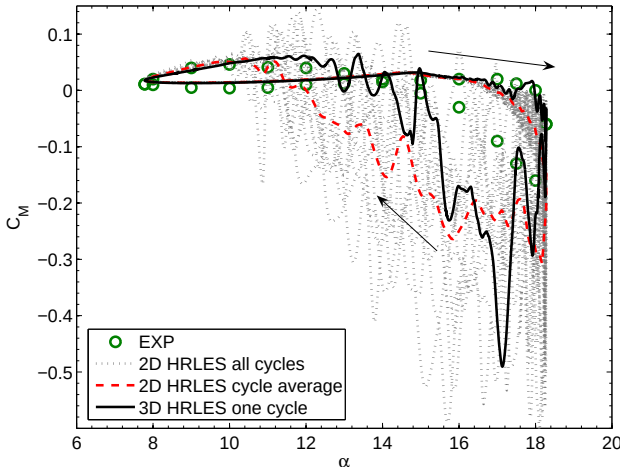

(c) Unsteady moment coefficient in oscillating motion.

Figure 11. Hysteresis of unsteady loads for deep dynamic stall. NACA 0015, $\alpha = 13.03 + 5.25\sin(\frac{2kU_\infty t}{C})$, $k = 0.1$, $M_\infty = 0.29$, $Re = 1.95 \times 10^6$, **2D and 3D results.**

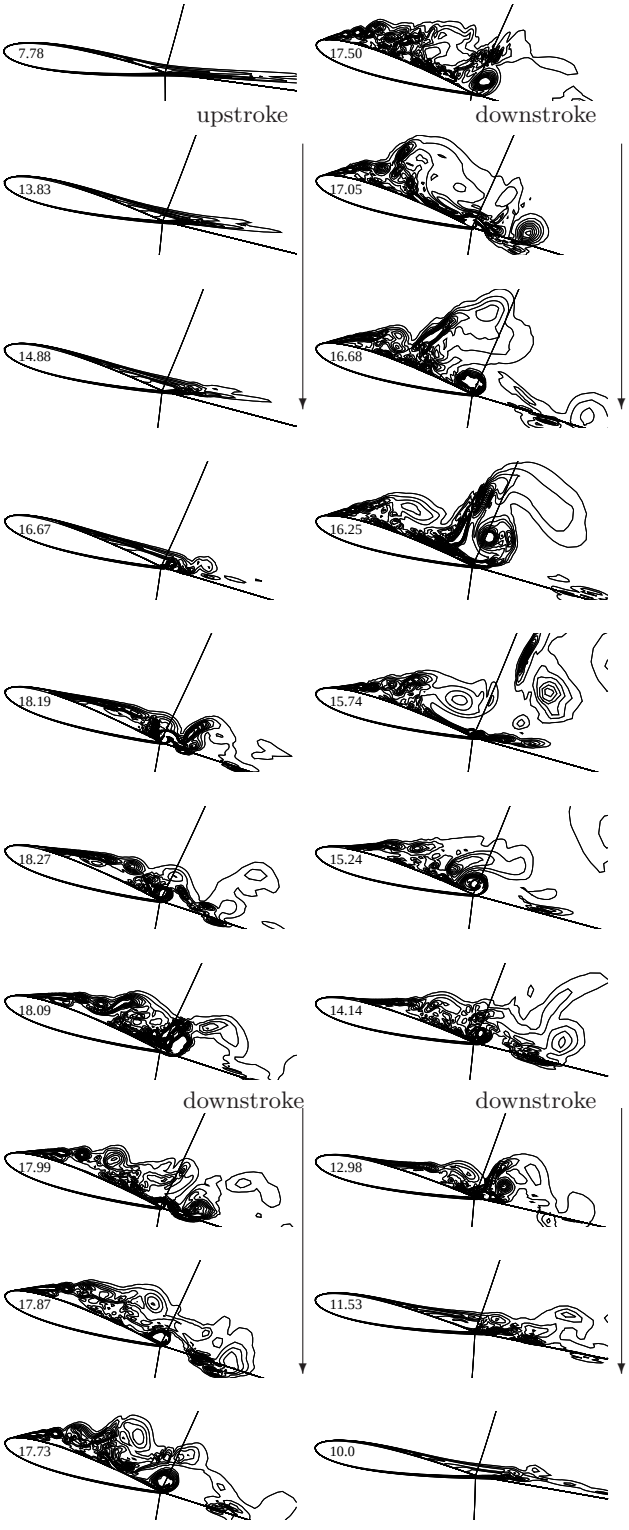

Figure 12. Instantaneous vorticity contours deep dynamic stall. NACA 0015, $\alpha = 13.03 + 5.25\sin(\frac{2kU_\infty t}{C})$, $k = 0.1$, $M_\infty = 0.29$, $Re = 1.95 \times 10^6$, **3D results.**

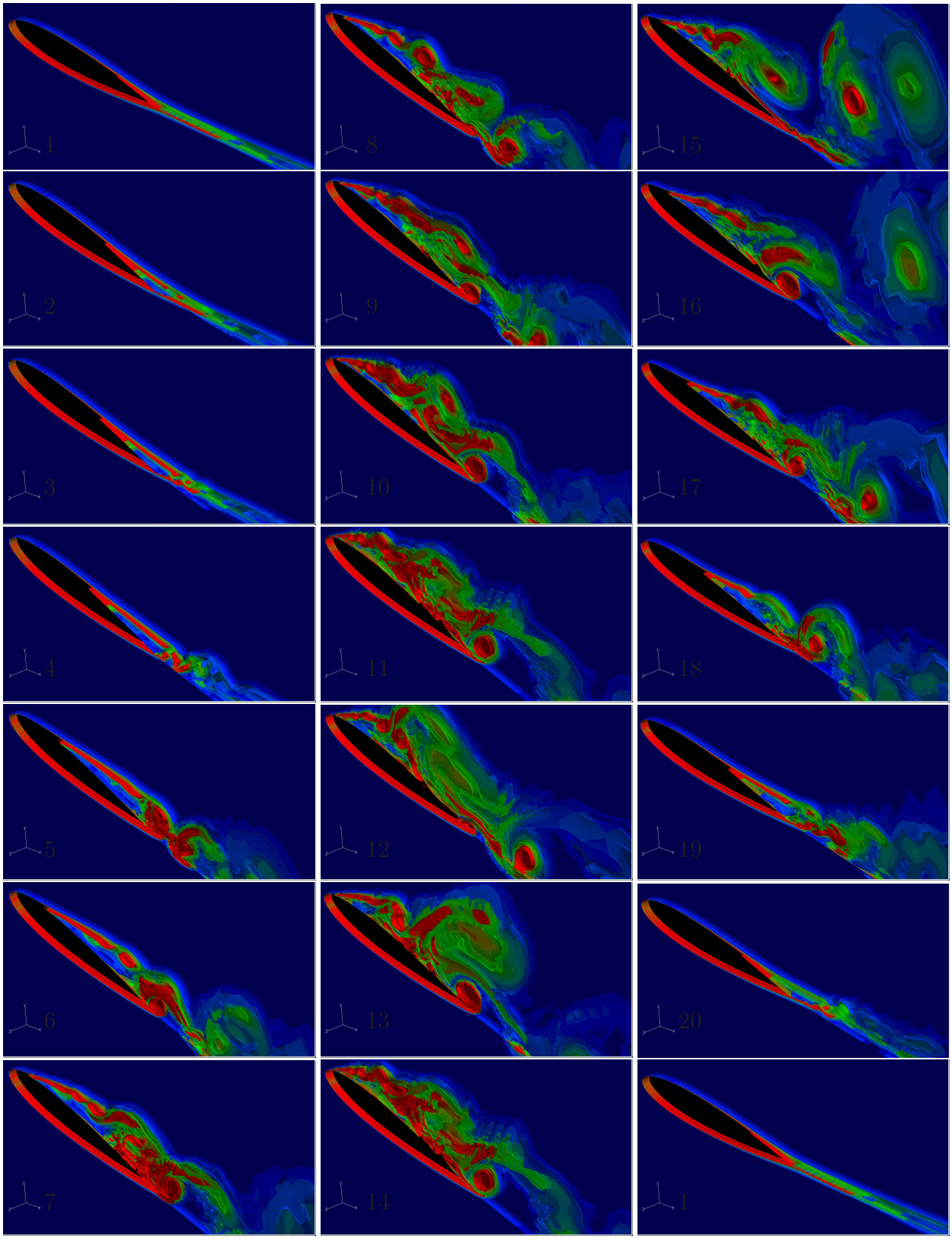

Figure 13. One cycle instantaneous snapshots. Isometric view of vorticity isosurfaces deep stall case. NACA 0015, $\alpha = 13.03 + 5.25\sin(\frac{2kU_\infty t}{C})$, $M_\infty = 0.29$, $Re = 1.95 \times 10^6$, **3D results.**

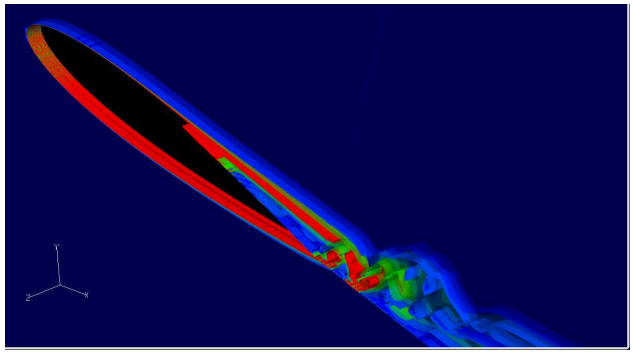

(a) Two dimensional wake during upstroke.

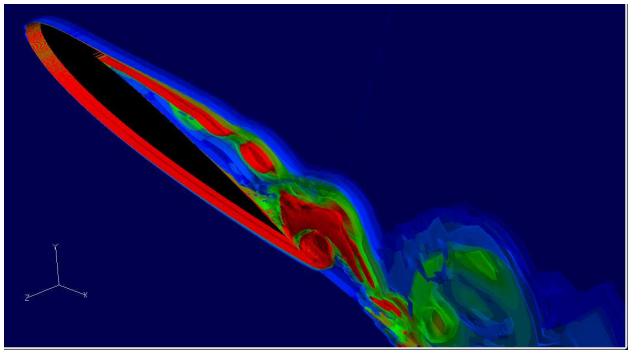

(b) Three dimensional instabilities in wake and trailing edge, upstroke.

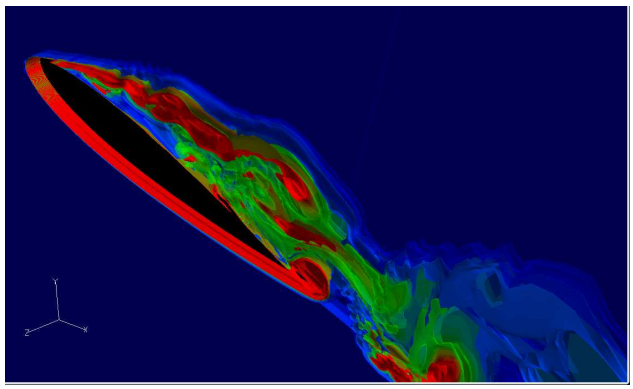

(c) Three dimensional instabilities in leading edge vorticity and 3D structures in wake and trailing edge, downstroke.

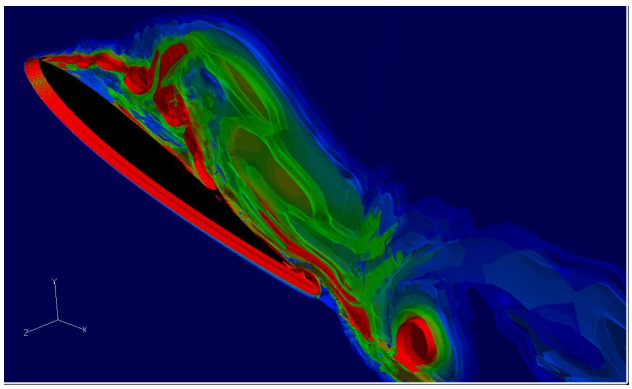

(d) Leading edge vortex shedding, downstroke.

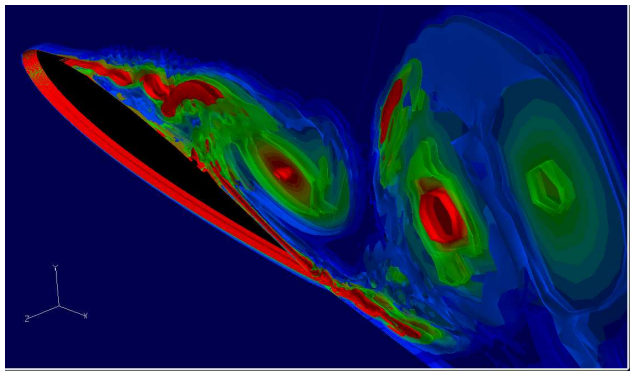

(e) Vortex shedding and vortex stretching during reattachments, downstroke.

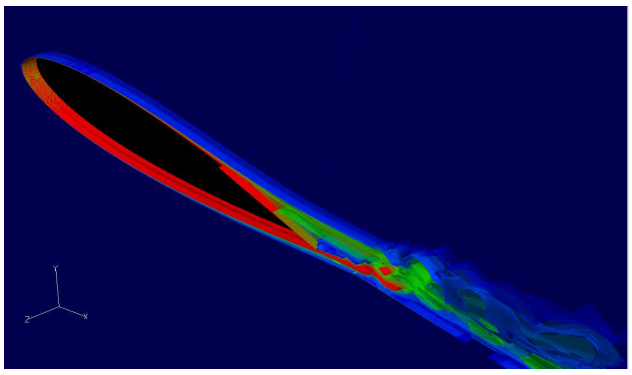

(f) Two dimensional flow, the wake still shows 3D instabilities.

Figure 14. Selected isometric view of vorticity isosurfaces deep stall case. NACA 0015, $\alpha = 13.03 + 5.25\sin(\frac{2kU_\infty t}{C})$**,** $M_\infty = 0.29$**,** $Re = 1.95 \times 10^6$**, 3D results.**

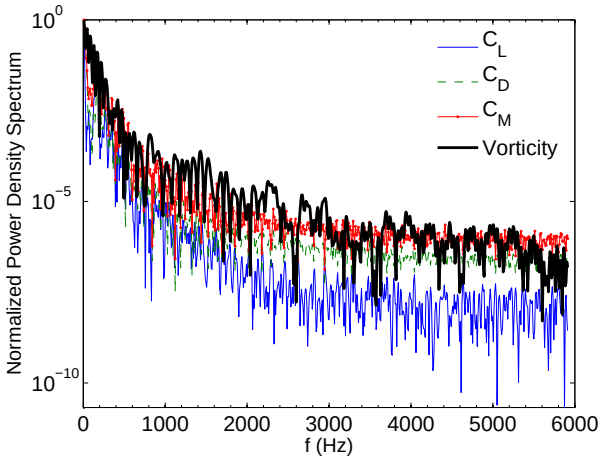

(a) Power density spectra of aerodynamic loads and vorticity magnitude at location 2.

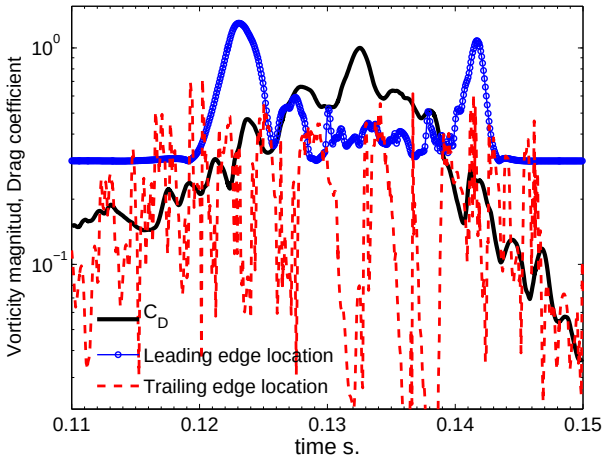

(b) Time signal of drag coefficient and vorticity magnitude at locations 1 and 2.

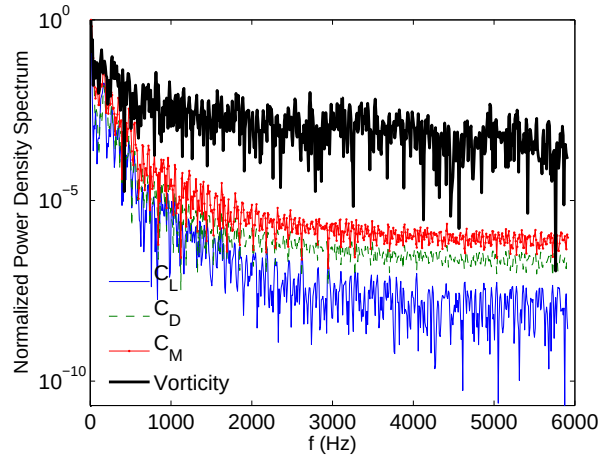

(c) Power density spectra of aerodynamic loads and vorticity magnitude at location 1.

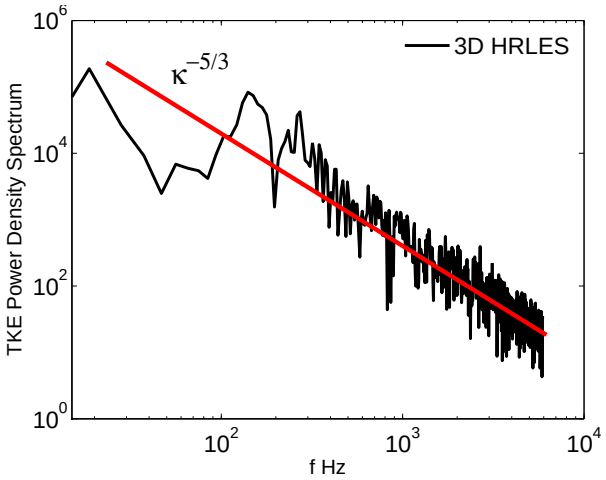

(d) Turbulent kinetic energy spectrum at location 1.

Figure 15. Power density spectrum of aerodynamic loads, vorticity magnitude and TKE. NACA 0015, $\alpha = 13.03 + 5.25\sin(\frac{2kU_\infty t}{C})$**,** $k = 0.1$**,** $M_\infty = 0.29$**,** $Re = 1.95 \times 10^6$**, 3D results.**